

Multiple- to single-gap superconductivity crossover in $\text{Nb}_5\text{Ir}_{3-x}\text{Pt}_x\text{O}$ alloys

Y. Xu,^{1,*} S. Jöhr,¹ L. Das,¹ J. Kitagawa,² M. Medarde,³ T. Shiroka,^{4,5} J. Chang,¹ and T. Shang^{1,3,†}

¹Physik-Institut, Universität Zürich, Winterthurerstrasse 190, CH-8057 Zürich, Switzerland

²Department of Electrical Engineering, Faculty of Engineering, Fukuoka Institute of Technology, 3-30-1 Wajiro-higashi, Higashi-ku, Fukuoka, 811-0295, Japan

³Laboratory for Multiscale Materials Experiments, Paul Scherrer Institut, Villigen CH-5232, Switzerland

⁴Laboratorium für Festkörperphysik, ETH Zürich, CH-8093 Zurich, Switzerland

⁵Paul Scherrer Institut, CH-5232 Villigen PSI, Switzerland

By using mostly the muon-spin rotation/relaxation (μSR) technique, we investigate the superconductivity (SC) of $\text{Nb}_5\text{Ir}_{3-x}\text{Pt}_x\text{O}$ ($x = 0$ and 1.6) alloys, with $T_c = 10.5$ K and 9.1 K, respectively. At a macroscopic level, their superconductivity was studied by electrical resistivity, magnetization, and specific-heat measurements. In both compounds, the electronic specific heat and the low-temperature superfluid density data suggest a nodeless SC. The superconducting gap value and the specific heat discontinuity at T_c are larger than that expected from the Bardeen-Cooper-Schrieffer theory in the weak-coupling regime, indicating strong-coupling superconductivity in the $\text{Nb}_5\text{Ir}_{3-x}\text{Pt}_x\text{O}$ family. In $\text{Nb}_5\text{Ir}_3\text{O}$, multigap SC is evidenced by the field dependence of the electronic specific heat coefficient and the superconducting Gaussian relaxation rate, as well as by the temperature dependence of the upper critical field. Pt substitution suppresses one of the gaps, and $\text{Nb}_5\text{Ir}_{1.4}\text{Pt}_{1.6}\text{O}$ becomes a single-gap superconductor. By combining our extensive experimental results, we provide evidence for a multiple- to single-gap SC crossover in the $\text{Nb}_5\text{Ir}_{3-x}\text{Pt}_x\text{O}$ family.

I. INTRODUCTION

The A_5B_3 compound family, where A is a transition or rare-earth metal, and B a (post)-transition metal or a metalloid element, consists of more than five hundreds compounds with three distinct crystal structures. They are orthorhombic Yb_5Sb_3 - ($Pnma$, No. 62), tetragonal Cr_5B_3 - ($I4/mcm$, No. 140), and hexagonal Mn_5Si_3 -type ($P6_3/mcm$, No. 193) structures. The latter possesses an interstitial $2b$ site, allowing the intercalation of light atoms, e.g., oxygen, boron, and carbon, to engineer the band topology. The ordered variant of Mn_5Si_3 -type structure is also known as Ti_5Ga_4 - or Hf_5CuSn_3 -type structure. To the latter belongs also $\text{Nb}_5\text{Ir}_3\text{O}$, whose crystal structure is presented in the inset of Fig. 1. Superconductivity (SC) has been reported to occur in several Ti_5Ga_4 -type compounds, including $\text{Nb}_5\text{Ir}_3\text{O}$ ¹, $(\text{Nb,Zr})_5\text{Pt}_3\text{O}$ ^{2,3}, $\text{Nb}_5\text{Ge}_3\text{C}_{0.3}$ ⁴, or $\text{Zr}_5\text{Pt}_3\text{C}_x$ ⁵, with the highest superconducting transition temperature T_c reaching ~ 15 K. Interestingly, specific heat and penetration depth results suggest a nodal superconducting gap in $\text{Zr}_5\text{Pt}_3\text{C}_x$ and possibly unconventional SC⁵.

The parent compound Nb_5Ir_3 consists of mixed tetragonal and hexagonal phases, both showing superconducting behavior below $T_c = 2.8$ and 9.4 K, respectively. The gradual intercalation of oxygen suppresses the tetragonal phase, making the hexagonal phase the dominant one. Accordingly, the T_c value increases linearly with the interstitial oxygen content, to reach 10.5 K in the purely hexagonal $\text{Nb}_5\text{Ir}_3\text{O}$ ¹. Nb_5Ir_3 exhibits an unusual interplay of electronegativity and SC states, whereas only SC remains in $\text{Nb}_5\text{Ir}_3\text{O}$ ¹. Density functional theory (DFT) calculations indicate Nb_5Ir_3 to be a multiband metal, whose density of states (DOS) at the Fermi level is dominated by the Nb $4d$ - and Ir $5d$ -orbitals¹. The increase of T_c in $\text{Nb}_5\text{Ir}_3\text{O}_x$ is most likely attributed to the enhanced electron-phonon coupling strength or to an increased DOS at the Fermi level (with extra Nb- $4d$ and O- $2p$ contributions)¹. On the other hand, by applying external pressure, T_c decreases monotonically from 10.5 K at ambient pressure to 9.5 K at 13 GPa^{1,6}. Unlike the $\text{Nb}_5\text{Ir}_3\text{O}_x$ case, in Zr_5Pt_3 the addition of oxygen reduces the T_c value from 6.4 K to 3.2 K (in $\text{Zr}_5\text{Pt}_3\text{O}_{0.6}$)³. Similarly, in Zr_5Sb_3 , the addition of oxygen reduces the T_c , with $\text{Zr}_5\text{Sb}_3\text{O}$ being a normal metal down to 1.8 K⁷.

Although the superconductivity of several Mn_5Si_3 - or

Ti_5Ga_4 -types of compounds has been studied by magnetic and transport measurements and, in many cases, electronic band-structure calculations are available, the microscopic nature of their superconducting phase remains largely unexplored. In $\text{Nb}_5\text{Ir}_3\text{O}$, the low- T electronic specific heat data suggest a nodeless SC with multiple gaps^{1,6}. While, in the $\text{Nb}_5\text{Pt}_3\text{O}$ case, the electronic specific heat shows a single-exponential temperature dependence below T_c , more consistent with a single-gap superconductivity². In $\text{Nb}_5\text{Ir}_{3-x}\text{Pt}_x\text{O}$, Pt substitution increases the a -axis lattice constant, while reducing the c -axis. As shown in Fig. 1, T_c is almost independent of Pt-content for $x \leq 0.5$, but it starts to decrease continuously for $x > 0.5$, reaching 4.3 K in $\text{Nb}_5\text{Pt}_3\text{O}$ ³. As hinted by specific heat data, one expects a crossover from multiple- to single gap SC in $\text{Nb}_5\text{Ir}_{3-x}\text{Pt}_x\text{O}$.

To provide further evidence for such a crossover, we initiated an extensive study of the superconducting properties of $\text{Nb}_5\text{Ir}_{3-x}\text{Pt}_x\text{O}$ for $x = 0$ and 1.6 , two representative cases in the multiple- and single gap regions (see arrows in Fig. 1), probing them at both the macroscopic and microscopic level. Both compounds were found to be fully-gapped superconductors, with $\text{Nb}_5\text{Ir}_3\text{O}$ showing multiple gaps and $\text{Nb}_5\text{Ir}_{1.4}\text{Pt}_{1.6}\text{O}$ being a single gap superconductor.

II. EXPERIMENTAL DETAILS

Polycrystalline samples of $\text{Nb}_5\text{Ir}_{3-x}\text{Pt}_x\text{O}$ were prepared by the arc-melting method (the full details are reported in Ref. 8). The magnetic susceptibility, electrical resistivity, and specific heat measurements were performed on a 7-T Quantum Design Magnetic Property Measurement System (MPMS-7) and a 9-T Physical Property Measurement System (PPMS-9). The muon-spin rotation/relaxation (μSR) experiments were carried out at the general purpose surface-muon (GPS) spectrometer at the Swiss muon source ($S\mu\text{S}$) at Paul Scherrer Institut, Villigen, Switzerland⁹. Both transverse-field (TF-) and zero-field (ZF-) μSR measurements were performed. The μSR data were analyzed using the `musrfit` software package¹⁰.

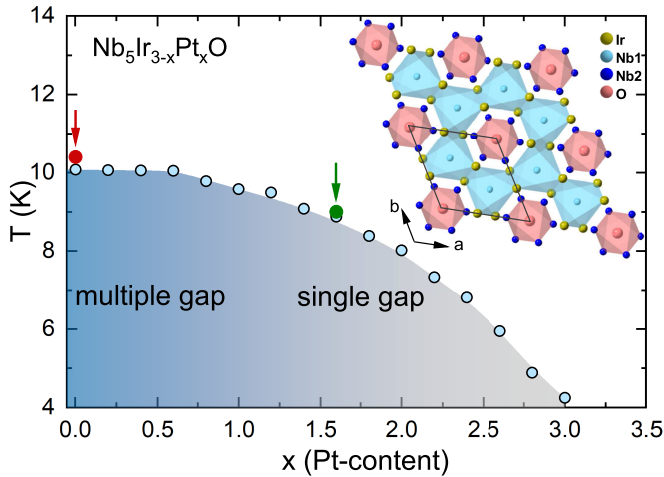


FIG. 1. The T - x phase diagram of $\text{Nb}_5\text{Ir}_{3-x}\text{Pt}_x\text{O}$. The arrows indicate the two samples studied here. The inset shows the crystal structure of $\text{Nb}_5\text{Ir}_3\text{O}$ viewed along the c -axis (solid lines mark the unit cell). A crossover from multiple- to single-gap SC with increasing Pt-content has been proposed. Data were adopted from Ref. 8.

III. RESULTS AND DISCUSSION

A. Magnetization

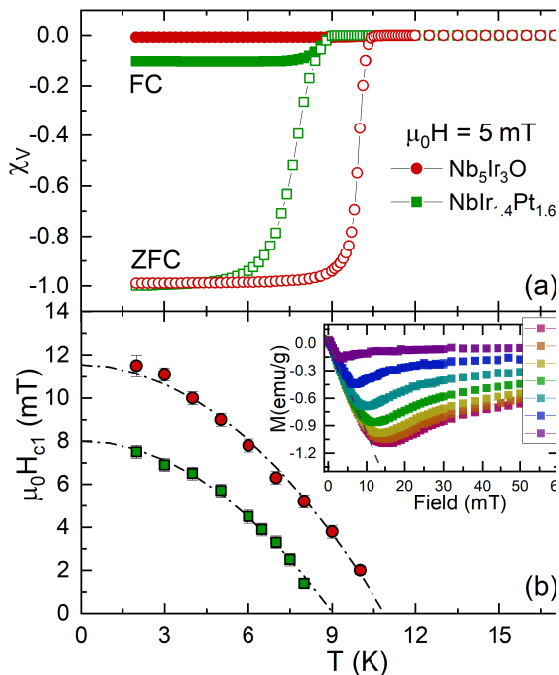


FIG. 2. (a) Temperature dependence of the magnetic susceptibility of $\text{Nb}_5\text{Ir}_3\text{O}$ and $\text{Nb}_5\text{Ir}_{1.4}\text{Pt}_{1.6}\text{O}$. (b) Estimated lower critical field $\mu_0 H_{c1}$ vs. temperature. The dash-dotted lines are fits to $\mu_0 H_{c1}(T) = \mu_0 H_{c1}(0)[1 - (T/T_c)^2]$. The inset shows the field-dependent magnetization $M(H)$ recorded at various temperatures up to T_c for $\text{Nb}_5\text{Ir}_{1.4}\text{Pt}_{1.6}\text{O}$. For each temperature, the lower critical field $\mu_0 H_{c1}$ was determined as the value where $M(H)$ starts deviating from linearity (dashed line). The magnetic susceptibilities were corrected by using the demagnetization factor obtained from the field-dependent magnetization at 2 K (base temperature).

The SC of $\text{Nb}_5\text{Ir}_{3-x}\text{Pt}_x\text{O}$ ($x = 0, 1.6$) was first characterized by magnetic susceptibility measurements, carried

out in a 5-mT field, using both field-cooled (FC) and zero-field-cooled (ZFC) protocols. As shown in Fig. 2(a), the ZFC-susceptibility, corrected to account for the demagnetization factor, indicates bulk SC below $T_c = 10.5$ K and 9.1 K for $\text{Nb}_5\text{Ir}_3\text{O}$ and $\text{Nb}_5\text{Ir}_{1.4}\text{Pt}_{1.6}\text{O}$, respectively. The well separated ZFC- and FC-susceptibilities indicate strong flux-line pinning across the $\text{Nb}_5\text{Ir}_{3-x}\text{Pt}_x\text{O}$ series. To perform TF- μSR measurements on superconductors, the applied magnetic field should exceed the lower critical field $\mu_0 H_{c1}$, so that the additional field-distribution broadening due to the flux-line lattice (FLL) can be quantified from the muon-spin relaxation rate. To determine $\mu_0 H_{c1}$, the field-dependent magnetization $M(H)$ was measured at various temperatures up to T_c . As an example, the $M(H)$ data for $\text{Nb}_5\text{Ir}_{1.4}\text{Pt}_{1.6}\text{O}$ are plotted in the inset of Fig. 2(b), with $\text{Nb}_5\text{Ir}_3\text{O}$ showing similar features. The estimated $\mu_0 H_{c1}$ values are summarized in Fig. 2(b) as a function of temperature for both samples. The dash-dotted lines represent fits to $\mu_0 H_{c1}(T) = \mu_0 H_{c1}(0)[1 - (T/T_c)^2]$ and yield lower critical fields of 11.5(2) and 8.0(1) mT for $\text{Nb}_5\text{Ir}_3\text{O}$ and $\text{Nb}_5\text{Ir}_{1.4}\text{Pt}_{1.6}\text{O}$, respectively.

B. Upper critical field

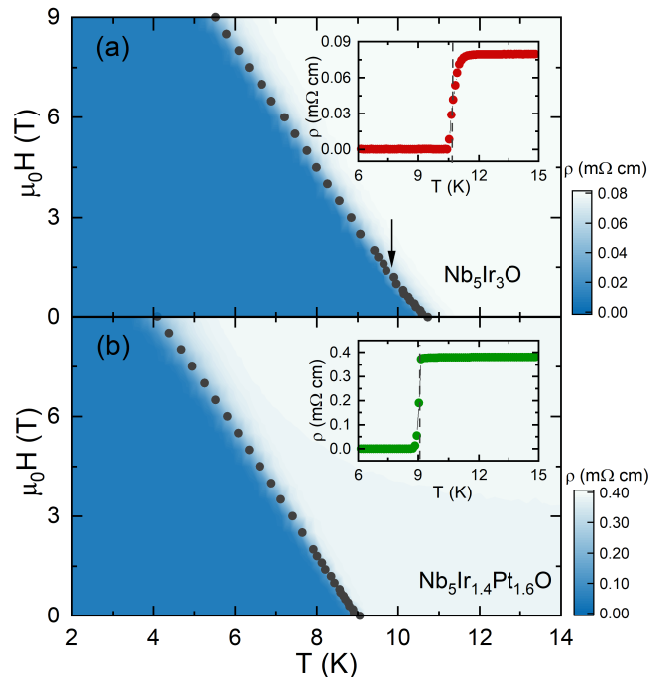


FIG. 3. Contour plots showing the electrical resistivity vs. temperature (down to 2 K) and magnetic field (up to 9 T) for $\text{Nb}_5\text{Ir}_3\text{O}$ (a) and $\text{Nb}_5\text{Ir}_{1.4}\text{Pt}_{1.6}\text{O}$ (b). Color hues represent the absolute value of electrical resistivity. The symbols indicate the critical temperatures T_c , as determined from the middle of superconducting transition (see dashed lines in the insets). Insets: In both cases, the zero-field electrical resistivity shows a sharp transition. The arrow in (a) indicates a change of slope (see also inset in Fig. 11).

The upper critical field $\mu_0 H_{c2}$ of $\text{Nb}_5\text{Ir}_{3-x}\text{Pt}_x\text{O}$ was determined from the measurements of electrical resistivity $\rho(T, H)$, specific heat $C(T, H)/T$, and magnetization $M(T, H)$ under various applied magnetic fields up to 9 T. Here we show $\rho(T, H)$ and $C(T, H)/T$ for both samples in Fig. 3 and Fig. 4, respectively. Upon applying a magnetic field, the superconducting transition, as detected using ei-

ther $\rho(T)$ or $C(T)/T$, shifts towards lower temperatures. The insets of Fig. 3 show the enlarged plot of zero-field electrical resistivity. $\text{Nb}_5\text{Ir}_3\text{O}$ exhibits an onset of the SC at $T_c^{\text{onset}} = 10.9\text{ K}$, and its resistivity drops to zero at $T_c^{\text{zero}} = 10.5\text{ K}$. For $\text{Nb}_5\text{Ir}_{1.4}\text{Pt}_{1.6}\text{O}$, $T_c^{\text{onset}} = 9.1\text{ K}$ and $T_c^{\text{zero}} = 8.9\text{ K}$. The sharp superconducting transitions ($\Delta T \sim 0.2\text{--}0.4\text{ K}$) in zero field, confirmed also by specific heat data (see Fig. 4), indicate the good quality of the samples.

The determined $\mu_0 H_{c2}$ values as a function of the reduced temperature $T_c/T_c(0)$ are summarized in Fig. 5. Here $T_c(0)$ is the transition temperature in zero field. For $\text{Nb}_5\text{Ir}_{1.4}\text{Pt}_{1.6}\text{O}$, the $\mu_0 H_{c2}$ values determined using different techniques are highly consistent. Conversely, for $\text{Nb}_5\text{Ir}_3\text{O}$, the datasets agree well only at low fields (below 2 T), since at higher fields the transition temperatures determined from $\rho(T)$ data are systematically higher than those derived from $C(T)/T$. The surface/filamentary SC above bulk T_c might cause the different T_c values, but why it shows up only in $\text{Nb}_5\text{Ir}_3\text{O}$ is not clear yet. The temperature dependence of $\mu_0 H_{c2}(T)$ was analyzed by means of Ginzburg-Landau- (GL)¹¹ and Werthamer-Helfand-Hohenberg (WHH) models¹². For $\text{Nb}_5\text{Ir}_3\text{O}$, the better agreement of the GL model with the data is clearly seen in Fig. 5(a). At low fields, both GL and WHH models reproduce very well the experimental data. However, at higher fields, the WHH model deviates significantly from the experimental data, giving underestimated values of $\mu_0 H_{c2}^{\text{WHH}}(0) = 9.3(1)\text{ T}$ and $12.4(1)\text{ T}$ for $C(T,H)/T$ and $\rho(T,H)$, respectively. In contrast, the GL model fits the data over the entire field range, providing $\mu_0 H_{c2}^{\text{GL}}(0) = 11.2(1)\text{ T}$ ($C(T)$) and $15.5(1)\text{ T}$ (ρ). In the case of $\text{Nb}_5\text{Ir}_{1.4}\text{Pt}_{1.6}\text{O}$, $\mu_0 H_{c2}(T)$ are reproduced very well by the WHH model, which yields $\mu_0 H_{c2}^{\text{WHH}}(0) = 12.7(1)\text{ T}$.

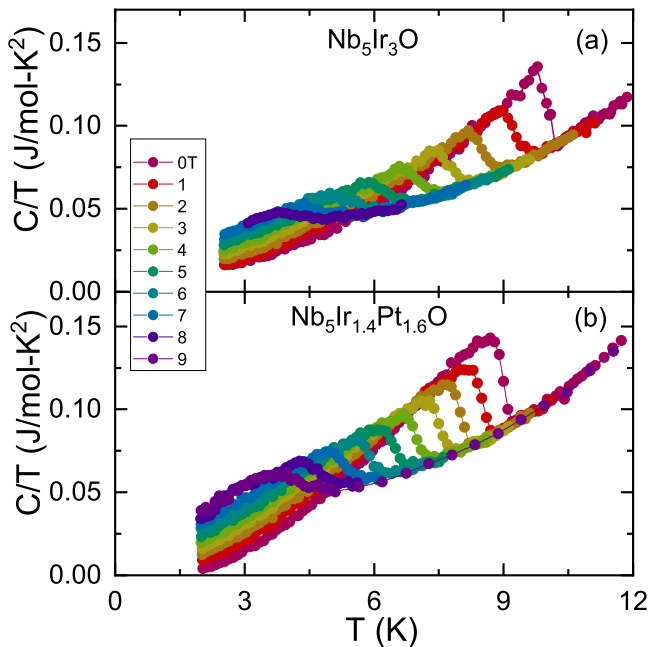


FIG. 4. Temperature dependence of the specific heat of $\text{Nb}_5\text{Ir}_3\text{O}$ (a) and $\text{Nb}_5\text{Ir}_{1.4}\text{Pt}_{1.6}\text{O}$ (b) measured under various magnetic fields up to 9 T. The data were collected upon sample heating.

The superconducting coherence length ξ can be calculated from $\xi = \sqrt{\Phi_0/2\pi H_{c2}}$, where $\Phi_0 = 2.07 \times 10^{-3}\text{ T}\mu\text{m}^2$ is the magnetic flux quantum. With a bulk $\mu_0 H_{c2}(0) = 11.2(1)$ and $12.7(1)\text{ T}$, the calculated $\xi(0)$ is $5.4(1)$ and

$5.1(1)\text{ nm}$ for $\text{Nb}_5\text{Ir}_3\text{O}$ and $\text{Nb}_5\text{Ir}_{1.4}\text{Pt}_{1.6}\text{O}$, respectively. The lower critical field $\mu_0 H_{c1}$ is related to the magnetic penetration depth λ and the coherence length ξ via $\mu_0 H_{c1} = (\Phi_0/4\pi\lambda^2)[\ln(\kappa) + 0.5]$, where $\kappa = \lambda/\xi$ is the GL parameter¹³. By using $\mu_0 H_{c1} = 11.5(2)\text{ mT}$ [$8.0(1)\text{ mT}$] and $\mu_0 H_{c2} = 11.2(1)\text{ T}$ [$12.7(1)\text{ T}$], the resulting magnetic penetration depth $\lambda_{\text{GL}} = 249(3)\text{ nm}$ [$308(3)\text{ nm}$] for $\text{Nb}_5\text{Ir}_3\text{O}$ ($\text{Nb}_5\text{Ir}_{1.4}\text{Pt}_{1.6}\text{O}$), is comparable to $230(2)\text{ nm}$ [$314(2)\text{ nm}$], the experimental values evaluated from TF- μSR data (see Sec. III D). A large GL parameter $\kappa \sim 50\text{--}60$, clearly indicates that $\text{Nb}_5\text{Ir}_{3-x}\text{Pt}_x\text{O}$ are type-II superconductors.

C. Zero-field specific heat

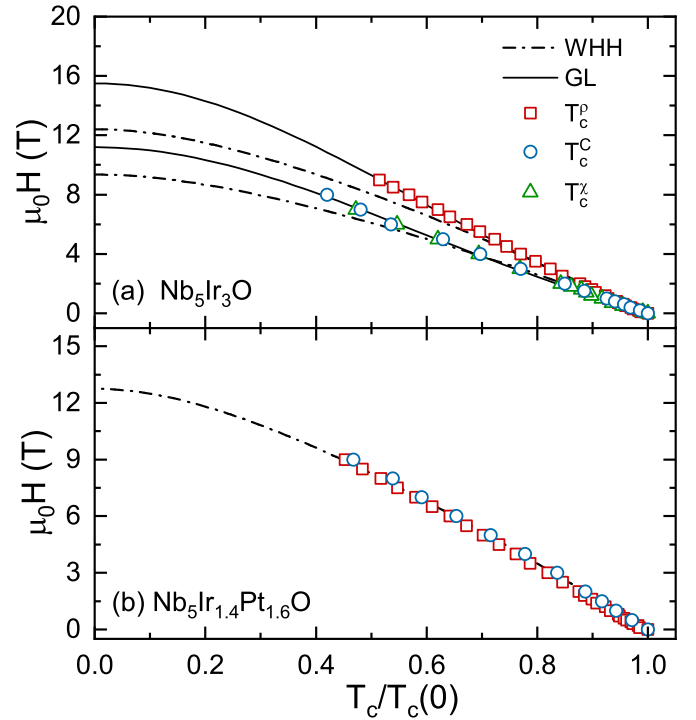


FIG. 5. Upper critical field $\mu_0 H_{c2}$ vs. reduced transition temperature $T_c/T_c(0)$ for $\text{Nb}_5\text{Ir}_3\text{O}$ (a) and $\text{Nb}_5\text{Ir}_{1.4}\text{Pt}_{1.6}\text{O}$ (b). The T_c values were determined from temperature-dependent electrical resistivity $\rho(T,H)$, magnetization $M(T,H)$, and specific heat $C(T,H)/T$. For $\rho(T,H)$ measurements, T_c is defined as the middle of the superconducting transition. Two different models, including GL- (solid lines) and WHH models (dash-dotted lines), were used to analyze the $\mu_0 H_{c2}(T)$ data. For the WHH model, the spin-orbit scattering was neglected.

The zero-field specific heat data in the low- T region (Fig. 6) show a sharp jump at T_c again indicating a bulk superconducting transition and a good sample quality. As shown in the inset, the normal-state specific heat data of $\text{Nb}_5\text{Ir}_{3-x}\text{Pt}_x\text{O}$ were fitted to $C/T = \gamma_n + \beta T^2 + \delta T^4$, where γ_n is the normal-state electronic specific heat coefficient, while the two other terms account for the phonon contribution to the specific heat. The derived values are $\gamma_n = 37(5)\text{ mJ/mol-K}^2$, $\beta = 0.32(9)\text{ mJ/mol-K}^4$ and $\delta = 1.7(3)\text{ }\mu\text{J/mol-K}^6$ for $\text{Nb}_5\text{Ir}_3\text{O}$, and $\gamma_n = 42(6)\text{ mJ/mol-K}^2$, $\beta = 0.36(13)\text{ mJ/mol-K}^4$ and $\delta = 2.6(5)\text{ }\mu\text{J/mol-K}^6$ for $\text{Nb}_5\text{Ir}_{1.4}\text{Pt}_{1.6}\text{O}$, respectively. Such large γ values suggest a relatively large effective electron mass (see Table I) and also strong electronic correlations in $\text{Nb}_5\text{Ir}_{3-x}\text{Pt}_x\text{O}$. The Debye

temperature can be estimated using $\Theta_D = (12\pi^4 Rn/5\beta)^{1/3}$, where $R = 8.314 \text{ J/mol}\cdot\text{K}$ is the molar gas constant and $n = 9$ is the number of atoms per formula unit, giving $\Theta_D = 380(7)$ and $365(8)$ K for $\text{Nb}_5\text{Ir}_3\text{O}$ and $\text{Nb}_5\text{Ir}_{1.4}\text{Pt}_{1.6}\text{O}$. The density of states at the Fermi level $N(\epsilon_F)$ is evaluated to be $N(\epsilon_F) = 3\gamma_n/(\pi^2 k_B^2) = 16(2)$ ($\text{Nb}_5\text{Ir}_3\text{O}$) and $18(2)$ states/eV-f.u. ($\text{Nb}_5\text{Ir}_{1.4}\text{Pt}_{1.6}\text{O}$)¹⁴, where k_B is the Boltzmann constant. Both values are comparable to those from the electronic band structure calculations¹. The electron-phonon coupling constant λ_{ep} , a measure of the attractive interaction between electrons due to phonons, was estimated using the semi-empirical McMillan formula¹⁵:

$$\lambda_{ep} = \frac{1.04 + \mu^* \ln(\Theta_D/1.45 T_c)}{(1 - 0.62\mu^*)\ln(\Theta_D/1.45 T_c) - 1.04}. \quad (1)$$

The Coulomb pseudo-potential μ^* is material-specific, typically lying in the $0.1 \leq \mu^* \leq 0.15$ range. Here, μ^* was fixed to 0.13, a typical value for metallic samples¹⁵. From Eq. (1) we obtain $\lambda_{ep} = 0.8(2)$ ($\text{Nb}_5\text{Ir}_3\text{O}$) and $0.7(3)$ ($\text{Nb}_5\text{Ir}_{1.4}\text{Pt}_{1.6}\text{O}$), which classifies both of them as relatively strongly coupled superconductors. This is consistent with previous results^{1,6}, and compatible with other strongly-coupled superconductors, as e.g. $\text{Ba}_{1-x}\text{K}_x\text{BiO}_3$ ($\lambda_{ep} \sim 1$), or $\text{W}_3\text{Al}_2\text{C}$ ($\lambda_{ep} \sim 0.78$)¹⁶⁻¹⁸.

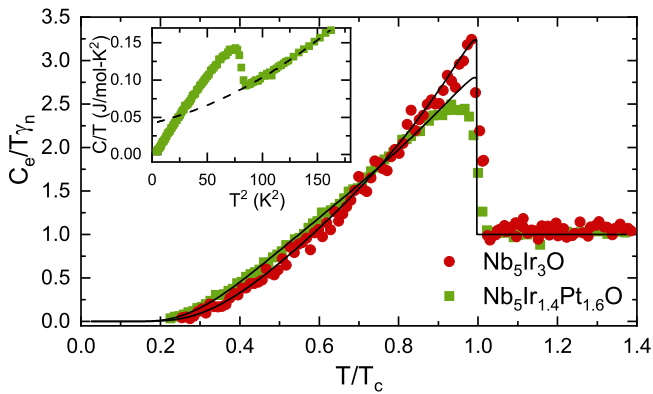


FIG. 6. Normalized electronic specific heat $C_e/\gamma_n T$ of $\text{Nb}_5\text{Ir}_3\text{O}$ and $\text{Nb}_5\text{Ir}_{1.4}\text{Pt}_{1.6}\text{O}$ as a function of the reduced temperature T/T_c . Inset: specific heat C/T vs. T^2 for $\text{Nb}_5\text{Ir}_{1.4}\text{Pt}_{1.6}\text{O}$; the dashed-line is a fit to $C/T = \gamma_n + \beta T^2 + \delta T^4$ for $T > T_c$. The solid lines in the main panel represent the electronic specific heat calculated by considering a fully-gapped s -wave model.

The electronic specific heat is obtained by subtracting the phonon contribution from the total specific heat. The main panel in Fig. 6 shows the temperature dependence of $C_e/\gamma_n T$, from which one can evaluate the discontinuity at T_c to be $\Delta C/\gamma T_c = 2.24(7)$ for $\text{Nb}_5\text{Ir}_3\text{O}$ and $1.50(5)$ for $\text{Nb}_5\text{Ir}_{1.4}\text{Pt}_{1.6}\text{O}$, both larger than the weak-coupling Bardeen-Cooper-Schrieffer (BCS) value of 1.43. The temperature evolution of the SC-related contribution to the entropy can be calculated from the BCS expression¹⁹:

$$S(T) = -\frac{6\gamma_n}{\pi^2 k_B} \int_0^\infty [f \ln f + (1-f) \ln(1-f)] d\epsilon, \quad (2)$$

where $f = (1 + e^{E/k_B T})^{-1}$ is the Fermi distribution and $E(\epsilon) = \sqrt{\epsilon^2 + \Delta^2(T)}$ is the excitation energy of quasiparticles, with ϵ the electron energy measured relative to the chemical potential (Fermi energy)^{19,20}. Here $\Delta(T) =$

$\Delta_0 \tanh\{1.82[1.018(T_c/T-1)]^{0.51}\}$ ²¹, with Δ_0 the zero temperature superconducting gap value. The electronic specific heat in the superconducting state can be calculated from $C_e = T \frac{dS}{dT}$. The solid lines in Fig. 6 are fits to the s -wave model with a single gap $\Delta_0 = 1.89(2)$ and $1.53(1)$ meV for $\text{Nb}_5\text{Ir}_3\text{O}$ and $\text{Nb}_5\text{Ir}_{1.4}\text{Pt}_{1.6}\text{O}$, respectively. Both gap values are consistent with the TF- μ SR results (see Fig. 8 below) and are larger than the standard BCS value ($\Delta_0 \sim 1.73 k_B T_c \sim 1.4$ meV) in the weak-coupling limit. This indicates strongly-coupled superconducting pairs in $\text{Nb}_5\text{Ir}_{3-x}\text{Pt}_x\text{O}$, consistent with the large λ_{ep} values. In previous studies, two superconducting gaps were required to describe the zero-field electronic specific heat at $T < 1/3 T_c$ ^{1,6}. Note, however, that the extra gap value was significantly smaller (< 0.02 meV) than the large gap and that it accounts for less than 10% of the total weights^{1,6}. As such, it can easily be influenced by disorder or oxygen content. In the case of our samples, a single gap could reproduce the electronic specific heat data very well over the whole temperature range. However, the field-dependent electronic specific heat coefficient, the TF- μ SR relaxation rates, and the temperature-dependent upper critical fields, all suggest multigap features in $\text{Nb}_5\text{Ir}_3\text{O}$, while $\text{Nb}_5\text{Ir}_{1.4}\text{Pt}_{1.6}\text{O}$ is a single gap superconductor (see details in Sec. III E).

D. Transverse-field μ SR

To investigate the superconducting properties of $\text{Nb}_5\text{Ir}_{3-x}\text{Pt}_x\text{O}$ at a microscopic level, TF- μ SR measurements were systematically carried out, covering both the normal and superconducting states. To track the additional field-distribution broadening due to the FLL in the mixed state, a magnetic field of 50 mT was applied in the normal state, before cooling the sample below T_c . The TF- μ SR time spectra were collected at various temperatures upon warming after the FC-protocol. Figure 7(a) shows two representative TF- μ SR spectra of $\text{Nb}_5\text{Ir}_3\text{O}$ collected at 1.6 K (i.e., below T_c) and 14 K (above T_c). In the normal state, the spectra show a relatively weak damping, reflecting a uniform field distribution. The enhanced depolarization rate in the superconducting state is attributed to the inhomogeneous field distribution due to the FLL, causing an additional field broadening in the mixed state. Such broadening is clearly demonstrated in Fig. 7(b), where the fast-Fourier-transform (FFT) spectra of the corresponding TF- μ SR data in Fig. 7(a) are shown. To account for the asymmetric field distribution in the superconducting state, the μ SR spectra were modeled by the following expression:

$$A_{\text{TF}}(t) = \sum_{i=1}^n A_i \cos(\gamma_\mu B_i t + \phi) e^{-\sigma_i^2 t^2/2} + A_{\text{bg}} \cos(\gamma_\mu B_{\text{bg}} t + \phi). \quad (3)$$

Here A_i (98%) and A_{bg} (2%) represent the initial muon-spin asymmetries for muons implanted in the sample and sample holder, respectively, with the latter not undergoing any depolarization. B_i and B_{bg} are the local fields sensed by implanted muons in the sample and sample holder, $\gamma_\mu = 2\pi \times 135.53 \text{ MHz/T}$ is the muon gyromagnetic ratio, ϕ is the shared initial phase, and σ_i is the Gaussian relaxation rate of the i th component. More than one oscillation is required to describe the TF- μ SR spectra of $\text{Nb}_5\text{Ir}_{3-x}\text{Pt}_x\text{O}$ samples. As illustrated in Fig. 7(b), at 1.6 K, two broad peaks can be clearly seen, below and above the applied magnetic

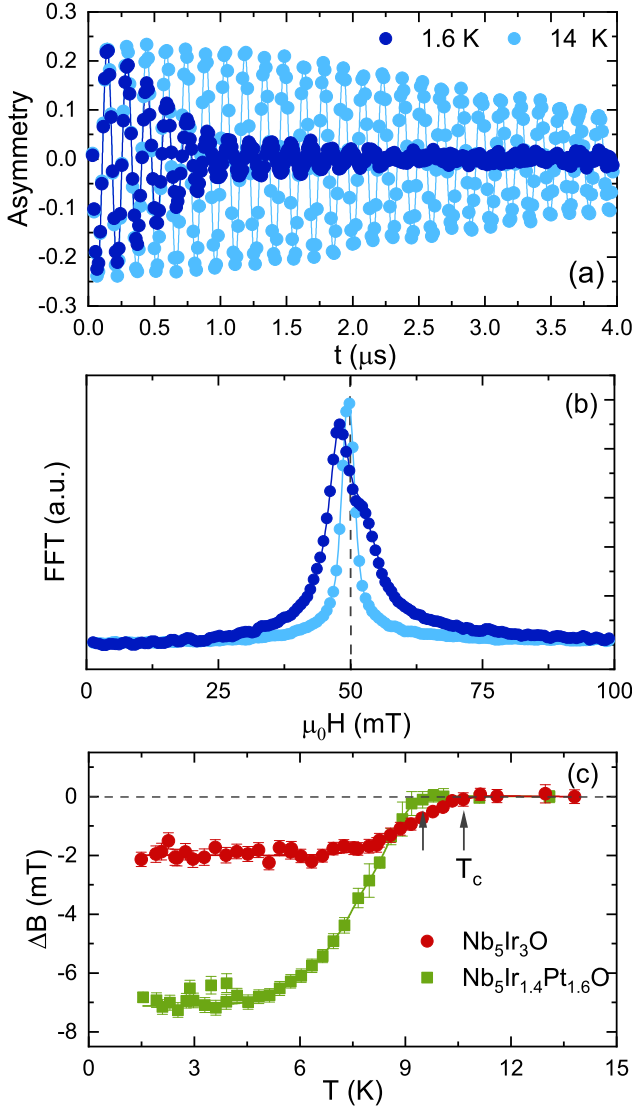


FIG. 7. (a) TF- μ SR time spectra collected at temperatures below (1.6 K) and above T_c (14 K) in an applied field of 50 mT for $\text{Nb}_5\text{Ir}_3\text{O}$. The fast Fourier transform of the TF- μ SR time spectra are shown in (b). Note that $\text{Nb}_5\text{Ir}_{1.4}\text{Pt}_{1.6}\text{O}$ exhibits similar spectra. Solid lines in (a) and (b) are fits to Eq. (3) using two Gaussian relaxations. The dashed vertical line indicates the applied magnetic field, showing a clear diamagnetic shift. (c) Diamagnetic shift ($\Delta B = \langle B \rangle - B_{\text{appl.}}$) vs. temperature for $\text{Nb}_5\text{Ir}_3\text{O}$ and $\text{Nb}_5\text{Ir}_{1.4}\text{Pt}_{1.6}\text{O}$.

field (50 mT). The solid lines in Figs. 7(a)-(b) represent fits to Eq. (3) with $n = 2$. Below T_c , a diamagnetic field shift appears in both samples [see Fig. 7(c)]. The relaxation rate is temperature-independent and small above T_c , but below T_c it starts to increase due to the onset of the FLL and the increased superfluid density (see insets in Fig. 8).

In the case of multi-component oscillations, the first-term in Eq. (3) describes the field distribution as a sum of n Gaussian relaxations (here $n = 2$)²²:

$$P(B) = \gamma_\mu \sum_{i=1}^2 \frac{A_i}{\sigma_i} \exp\left[-\frac{\gamma_\mu^2 (B - B_i)^2}{2\sigma_i^2}\right]. \quad (4)$$

The first- and second moments of the field distribution can

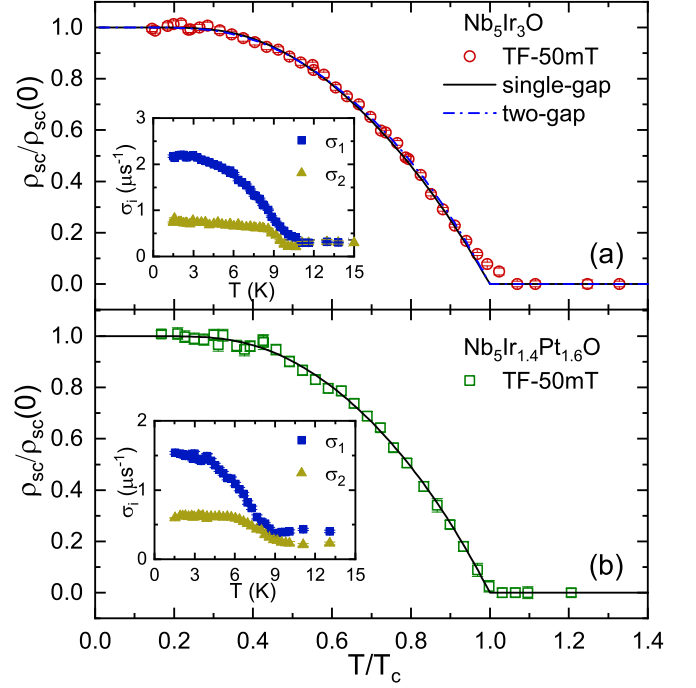


FIG. 8. Superfluid density vs. reduced temperature T/T_c , as determined from TF- μ SR measurements in an applied magnetic field of 50 mT for $\text{Nb}_5\text{Ir}_3\text{O}$ (a) and $\text{Nb}_5\text{Ir}_{1.4}\text{Pt}_{1.6}\text{O}$ (b). The insets show the temperature dependence of the muon-spin relaxation rate $\sigma_i(T)$. The lines through the data represent fits to a fully-gapped s -wave model with either a single gap (solid) or two gaps (dash-dotted). The goodness of fit are $\chi_r^2 = 3.8$ (single-gap model) and 3.2 (two-gap model), respectively.

be calculated by:

$$\langle B \rangle = \sum_{i=1}^2 \frac{A_i B_i}{A_{\text{tot}}}, \quad \text{and} \quad (5)$$

$$\langle B^2 \rangle = \frac{\sigma_{\text{eff}}^2}{\gamma_\mu^2} = \sum_{i=1}^2 \frac{A_i}{A_{\text{tot}}} \left[\frac{\sigma_i^2}{\gamma_\mu^2} + (B_i - \langle B \rangle)^2 \right],$$

where $A_{\text{tot}} = A_1 + A_2$. The superconducting Gaussian relaxation rate σ_{sc} can be extracted by subtracting the nuclear contribution according to $\sigma_{\text{sc}} = \sqrt{\sigma_{\text{eff}}^2 - \sigma_n^2}$, where σ_n is the nuclear relaxation rate, assumed to be temperature independent in such a narrow temperature range (see also ZF- μ SR below).

Since the upper critical fields of $\text{Nb}_5\text{Ir}_{3-x}\text{Pt}_x\text{O}$ (see Fig. 5) are significantly higher than the transverse field used in the μ SR measurements (here, 50 mT), the magnetic penetration depth $\lambda(T)$ and the superfluid density $\rho_{\text{sc}}(T)$ [$\propto \lambda^{-2}(T)$] can be obtained from $\sigma_{\text{sc}}(T)$ according to^{13,23}:

$$\frac{\sigma_{\text{sc}}^2(T)}{\gamma_\mu^2} = 0.00371 \frac{\Phi_0^2}{\lambda^4(T)}. \quad (6)$$

The derived superfluid density normalized to the zero-temperature values is shown in the main panels of Fig. 8. The superfluid density is almost constant at temperatures below $T_c/3$, indicating fully-gapped SC in $\text{Nb}_5\text{Ir}_{3-x}\text{Pt}_x\text{O}$, in good agreement with the specific heat results (see Fig. 6).

For a more quantitative insight into the SC of $\text{Nb}_5\text{Ir}_{3-x}\text{Pt}_x\text{O}$, the derived superfluid density $\rho_{\text{sc}}(T)$ was further an-

alyzed by using a fully-gapped s -wave model:

$$\frac{\lambda^{-2}(T)}{\lambda_0^{-2}} = \frac{\rho_{sc}(T)}{\rho_{sc}(0)} = 1 + 2 \int_{\Delta(T)}^{\infty} \frac{E}{\sqrt{E^2 - \Delta^2(T)}} \frac{\partial f}{\partial E} dE. \quad (7)$$

Here f and $\Delta(T)$ are the Fermi and superconducting gap functions (see details in Sec. III C). The solid black lines in Fig. 8 are fits to the above model with a single gap, which yield zero-temperature gap values $\Delta_0 = 1.79(3)$ and $1.67(2)$ meV, and magnetic penetration depths $\lambda_0 = 230(2)$ and $314(2)$ nm, for $\text{Nb}_5\text{Ir}_3\text{O}$ and $\text{Nb}_5\text{Ir}_{1.4}\text{Pt}_{1.6}\text{O}$, respectively. The estimated BCS coherence length ξ_0 is larger than the electronic mean free path l_e (see Table I), implying the samples are in the dirty limit. Therefore, the temperature-dependent superfluid density was also analyzed using a dirty-limit model. In this case, in the BCS approximation, the temperature dependence of the superfluid density is given by $\rho_{sc}(T) = \frac{\Delta(T)}{\Delta_0} \tanh\left[\frac{\Delta(T)}{2k_B T}\right]$ ¹⁹, which yields a gap value of $1.61(3)$ and $1.51(3)$ meV, slightly smaller than the clean-limit value, but still larger than the weak-coupling BCS value. In the $\text{Nb}_5\text{Ir}_3\text{O}$ case, to compare the zero-field electronic specific heat results^{1,6} with those from μSR , the superfluid density was also analyzed using a two-gap model^{21,24,25}. As shown by the blue dash-dotted line in Fig. 8 (a), the two-gap model shows a slightly better agreement with the $\rho_{sc}(T)$ data, as confirmed by the smaller χ_r^2 value. The derived gap values are $\Delta_0^s = 1.34(3)$ meV (small) and $\Delta_0^l = 1.97(3)$ meV (large), with a weight $w = 0.2$ of the small gap. Such a small weight makes the multi-gap features barely visible in the $\rho_{sc}(T)$ or C_e/T data. Although the $\rho_{sc}(T)$ data can be well described by an s -wave model with either single- or two gaps, the latter is more consistent with the field-dependent electronic specific heat coefficient (Fig. 9), the superconducting Gaussian relaxation rate (Fig. 10), the upper critical field (Fig. 11), and the electronic band structure calculations¹.

E. Evidence of multigap superconductivity in $\text{Nb}_5\text{Ir}_3\text{O}$

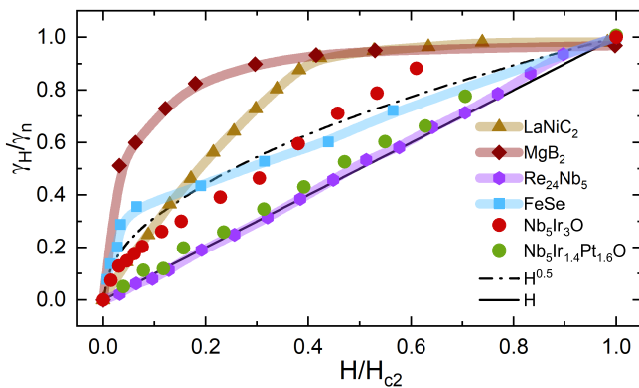


FIG. 9. The normalized specific heat coefficient γ_H/γ_n vs. the reduced magnetic field $H/H_{c2}(0)$ for $\text{Nb}_5\text{Ir}_{3-x}\text{Pt}_x\text{O}$. γ_H is obtained as the linear extrapolation of C/T vs. T^2 (in the superconducting phase) to zero temperature. The solid line indicates a linear dependence, as predicted for a single-gap s -wave gap structure, the dash-dotted line represents the dependence expected for an anisotropic gap or a gap with nodes, e.g., d -wave. The data of the reference samples are adopted from Refs. 26–29.

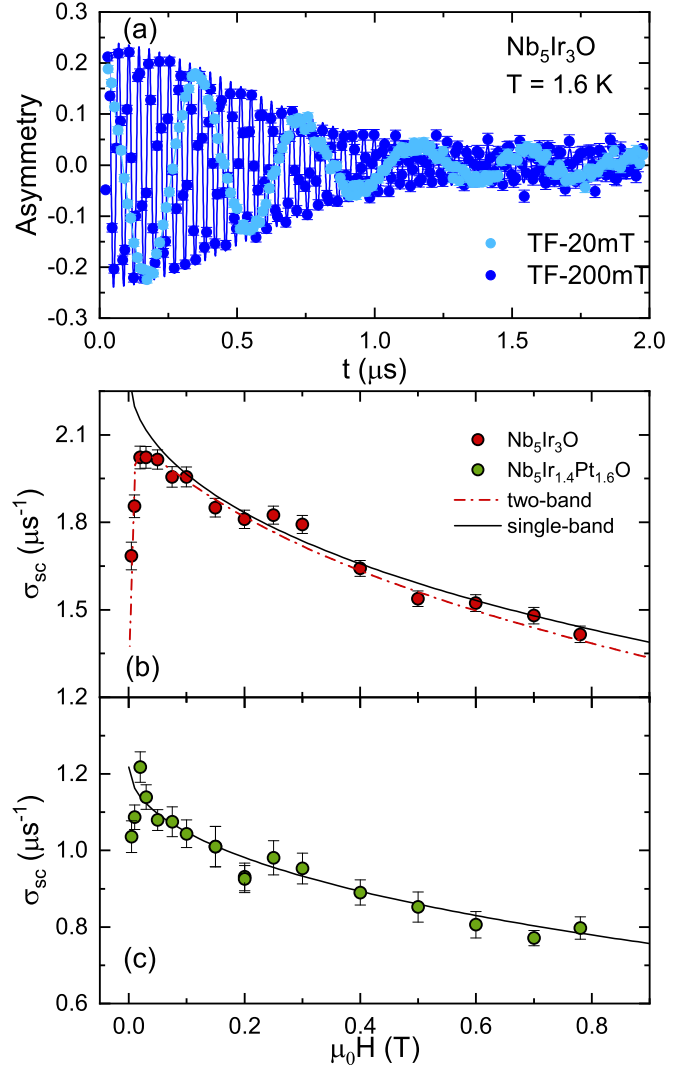


FIG. 10. (a) TF- μSR time spectra for $\text{Nb}_5\text{Ir}_3\text{O}$ measured at $T = 1.5$ K (superconducting state) in a field of 20 and 200 mT. $\text{Nb}_5\text{Ir}_{1.4}\text{Pt}_{1.6}\text{O}$, too, shows a similar behavior. Field-dependent superconducting Gaussian relaxation rate $\sigma_{sc}(H)$ for $\text{Nb}_5\text{Ir}_3\text{O}$ (b) and $\text{Nb}_5\text{Ir}_{1.4}\text{Pt}_{1.6}\text{O}$ (c). The dash-dotted and solid lines represent fits to two-band and single-band models, respectively. The goodness of fit are $\chi_r^2 = 1.17$ (two-band model) and 2.65 (single-band model) for $\text{Nb}_5\text{Ir}_3\text{O}$, and $\chi_r^2 = 1.15$ for $\text{Nb}_5\text{Ir}_{1.4}\text{Pt}_{1.6}\text{O}$ (single-band model). The data for $H < H_{c1}$ are excluded to evaluate the χ_r^2 value.

The multigap nature of $\text{Nb}_5\text{Ir}_3\text{O}$ superconductivity can be further inferred from the field-dependent electronic specific heat coefficient $\gamma_H(H)$. The normalized values γ_H/γ_n vs. the reduced magnetic field $H/H_{c2}(0)$ are shown in Fig. 9 (here γ_n is the zero-field normal-state value). For $\text{Nb}_5\text{Ir}_3\text{O}$, due to its multigap nature, it is difficult to describe the field dependence with a simple formula. $\gamma_H(H)$ clearly deviates from the linear field dependence (solid line) expected for single gap fully-gapped superconductors³⁰, or from the square-root dependence \sqrt{H} (dash-dotted line), expected for nodal superconductors^{31,32}. Different from the case of $\text{Nb}_5\text{Ir}_3\text{O}$, but similar to $\text{Re}_{24}\text{Nb}_5$ ²⁹, $\gamma_H(H)$ of $\text{Nb}_5\text{Ir}_{1.4}\text{Pt}_{1.6}\text{O}$ is practically linear in field, more consistent with a single gap SC. $\text{Nb}_5\text{Ir}_3\text{O}$ instead exhibits features similar to other well studied multigap superconductors, as e.g., LaNiC_2 ²⁶, FeSe ²⁷, and MgB_2 ²⁸, although the slopes of $\gamma_H(H)$ close to zero field are different, reflecting the different magnitudes

and weights of the smaller gap.

To get further insight into the multigap SC of $\text{Nb}_5\text{Ir}_3\text{O}$, TF- μSR measurements were performed in different magnetic fields up to 780 mT at base temperature (1.6 K) in both samples. Figure 10(a) shows the TF- μSR spectra of $\text{Nb}_5\text{Ir}_3\text{O}$, collected at 20 and 200 mT, with the spectra in other applied fields and in $\text{Nb}_5\text{Ir}_{1.4}\text{Pt}_{1.6}$ showing similar features. The spectra were analyzed using the same model as described in Eq. (3), and the resulting superconducting Gaussian relaxation rates σ_{sc} versus the applied magnetic field are summarized in Fig. 10(b) ($\text{Nb}_5\text{Ir}_3\text{O}$) and Fig. 10(c) ($\text{Nb}_5\text{Ir}_{1.4}\text{Pt}_{1.6}$). $\sigma_{\text{sc}}(H)$ was analyzed using both a single- and a two-band model. In the latter case, each band is characterized by its own superconducting coherence length [i.e., $\xi_1(0)$ and $\xi_2(0)$] and a weight w accounting for the contribution of the second band [$\xi_2(0)$] to the total superfluid density, similar to the two-gap model in Fig. 8(a). The details of the single- and two-band models can be found in Refs. 33 and 34. By fixing $w = 0.2$ and $\xi_1(0) = 5.4$ nm, as estimated from the analysis of $\rho_{\text{sc}}(T)$ (Fig. 8) and of the upper critical field (Fig. 5), we obtain the dash-dotted line fit in Fig. 10(b), which provides $\lambda_0 = 222(3)$ nm and $\xi_2(0) = 14(1)$ nm. The derived λ_0 is consistent with the value (230 nm) estimated from the analysis of $\rho_{\text{sc}}(T)$ in Fig. 8(a). The upper critical field of 1.7(2) T calculated from the coherence length of the second band $\xi_2(0)$ is also in good agreement with the field values where $\gamma_{\text{H}}(H)$ and $\mu_0 H_{\text{c}2}(T)$ change their slope, as shown by the arrows in Fig. 3(a) and the inset in Fig. 11. While the single-band model reproduces very well the $\sigma_{\text{sc}}(H)$ data for $\text{Nb}_5\text{Ir}_{1.4}\text{Pt}_{1.6}$ [see Fig 10(c)], it is less satisfactory for $\text{Nb}_5\text{Ir}_3\text{O}$, where a two-band model is required to obtain a similarly small χ^2_{r} value [see Fig 10(b)].

A positive curvature of the upper critical field near T_{c} is considered a typical feature of multiband superconductors, as e.g., MgB_2 ^{35,36}. It reflects the gradual suppression of the small superconducting gap with increasing magnetic field. Indeed, in $\text{Nb}_5\text{Ir}_3\text{O}$, $\mu_0 H_{\text{c}2}(T)$ exhibits a clear kink close to 1.5 T [see arrow in Fig. 3(a)], which coincides with the field value which suppresses the small superconducting gap. This is reflected also in the derivative of $\mu_0 H_{\text{c}2}(T)$ with respect to temperature (see arrow in the inset of Fig. 11). Also $\gamma_{\text{H}}(H)$ changes its slope near this critical field (close to 0.1 in Fig. 9). Since, in $\text{Nb}_5\text{Ir}_{1.4}\text{Pt}_{1.6}\text{O}$, the small gap is already suppressed by Pt substitution, it exhibits a linear field dependence of $\gamma_{\text{H}}(H)$ (Fig. 9), consistent with a fully-gapped SC with a single gap. As shown in Fig. 11, the upper critical field of $\text{Nb}_5\text{Ir}_3\text{O}$ was also analyzed by a two-band model³⁷, from which we estimate the upper critical field values $\mu_0 H_{\text{c}2}(0) = 13.1(1)$ [from $C(T, H)$ or $M(T, H)$] and 18.5(1) T [from $\rho(T, H)$], both consistent with the GL model in Fig. 5(a).

E Uemura plot

According to the ratio of T_{c} to the effective Fermi temperature T_{F} , the different classes of superconductors can be classified following the so-called Uemura plot³⁹. As seen in Fig. 12, conventional BCS superconductors exhibit $T_{\text{c}}/T_{\text{F}} < 10^{-3}$, here exemplified by the elemental Sn, Al, and Zn superconductors. In contrast, as indicated by the shaded region, several types of unconventional superconductors, including heavy-fermions, organic superconductors, iron pnictides and cuprates, all lie within a $10^{-2} < T_{\text{c}}/T_{\text{F}} <$

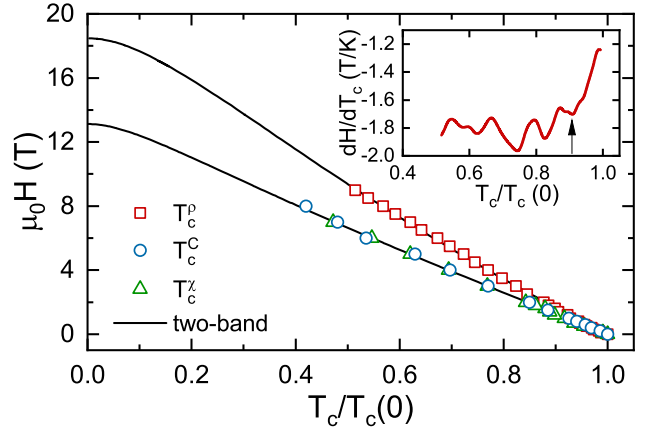


FIG. 11. Upper critical field $\mu_0 H_{\text{c}2}$ vs. reduced transition temperature $T_{\text{c}}/T_{\text{c}}(0)$ for $\text{Nb}_5\text{Ir}_3\text{O}$ [same as in Fig. 5(a)]. The solid lines are fits using a two-band model. Inset: Temperature derivative of the upper critical field, as determined from the electrical resistivity.

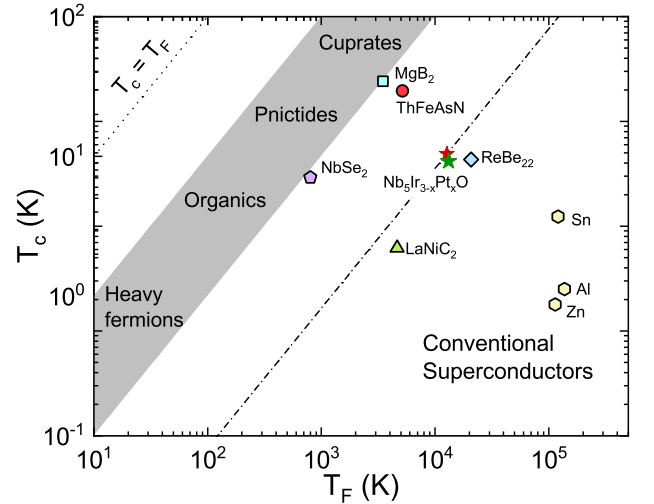


FIG. 12. Uemura plot showing T_{c} against the effective Fermi temperature T_{F} for various superconductors. The shaded region, with $1/100 < T_{\text{c}}/T_{\text{F}} < 1/10$, indicates the band of unconventional superconductors, such as heavy fermions, organic superconductors, iron pnictides and cuprates. The dotted line corresponds to $T_{\text{c}} = T_{\text{F}}$, while the dash-dotted line indicates $T_{\text{c}}/T_{\text{F}} = 8.2 \times 10^{-4}$ for $\text{Nb}_5\text{Ir}_3\text{O}$. The data of the reference samples were adopted from Refs. 25, 29, 38–40.

10^{-1} band. Between these two categories are located several multigap superconductors, as e.g., LaNiC_2 , NbSe_2 and MgB_2 . According to the superconducting parameters obtained from the measurements presented here (see details in Table I), the calculated $T_{\text{c}}/T_{\text{F}}$ values for $\text{Nb}_5\text{Ir}_3\text{O}$ and $\text{Nb}_5\text{Ir}_{1.4}\text{Pt}_{1.6}\text{O}$ are $\sim 8.2\text{--}8.4 \times 10^{-4}$ (see star symbols in Fig. 12). Although there is no evidence for them to be classified as unconventional superconductors, the $\text{Nb}_5\text{Ir}_{3-x}\text{Pt}_x\text{O}$ family is clearly far off the conventional superconductors and it shows similar ratios to other multigap superconductors, such as LaNiC_2 and ReBe_{22} (both located near the dash-dotted line).

Table I. Normal- and superconducting state properties of $\text{Nb}_5\text{Ir}_3\text{O}$ and $\text{Nb}_5\text{Ir}_{1.4}\text{Pt}_{1.6}\text{O}$, as determined from electrical resistivity, magnetic susceptibility, specific heat, and μSR measurements. The London penetration depth λ_L , the effective mass m^* , carrier density n_s , BCS coherence length ξ_0 , electronic mean-free path l_e , Fermi velocity v_F , and effective Fermi temperature T_F were estimated following equations in Ref. 41.

Property	Unit	$\text{Nb}_5\text{Ir}_3\text{O}$	$\text{Nb}_5\text{Ir}_{1.4}\text{Pt}_{1.6}\text{O}$
T_c^a	K	10.5(1)	9.1(1)
$\mu_0 H_{c1}$	mT	11.5(2)	8.0(1)
$\mu_0 H_{c1}^{\mu\text{SR}}$	mT	13.3(1)	7.7(1)
$\mu_0 H_{c2}^\rho$	T	15.5(1)	12.7(1)
$\mu_0 H_{c2}^C$	T	11.2(1)	12.7(1)
γ_n	mJ/mol-K ²	37(5)	42(6)
Θ_D^C	K	379(30)	368(30)
λ_{ep}	—	0.8(2)	0.73(25)
$N(\epsilon_F)$	states/eV-f.u.	16(2)	18(2)
$\Delta_0^{\mu\text{SR}}(\text{clean})$	meV	1.79(3) ^b	1.67(2)
$\Delta_0^{\mu\text{SR}}(\text{dirty})$	meV	1.61(3)	1.51(3)
Δ_0^C	meV	1.89(2)	1.53(1)
$\Delta C/\gamma_n T_c$	—	2.24(7)	1.50(5)
$\lambda_0^{\mu\text{SR}}$	nm	230(2)	314(2)
λ_{GL}	nm	249(3)	308(3)
λ_L	nm	73(5)	81(9)
$\xi(0)$	nm	5.4(1)	5.1(1)
κ	—	50(3)	60(3)
m^*	m_e	8.0(8)	9.2(4)
n_s	10^{28} m^{-3}	4.2(5)	3.9(7)
ξ_0	nm	18(1)	16(2)
l_e	nm	2.1(1)	1.2(1)
ξ_0/l_e	—	9(1)	14(2)
v_F	10^5 ms^{-1}	1.5(1)	1.3(1)
T_F	10^4 K	1.27(5)	1.1(1)

^a Similar values were determined via electrical resistivity, magnetic susceptibility, and specific heat measurements.

^b The two-gap model provides an averaged gap value of 1.84(3) meV.

G. Zero-field μSR

ZF- μSR measurements were also performed in the normal- and superconducting states to search for possible magnetism or time-reversal symmetry breaking in the superconducting state of $\text{Nb}_5\text{Ir}_{3-x}\text{Pt}_x\text{O}$. Representative ZF- μSR spectra collected above (15 K) and below T_c (1.6 K) for $\text{Nb}_5\text{Ir}_{3-x}\text{Pt}_x\text{O}$ are shown in Fig. 13. Neither coherent oscillations nor fast damping could be identified at either temperature, implying the lack of any magnetic order/fluctuations in $\text{Nb}_5\text{Ir}_{3-x}\text{Pt}_x\text{O}$. Therefore, in absence of an applied magnetic field, the weak muon-spin relaxation is mainly determined by the randomly oriented nuclear moments, which can be modeled by a Gaussian Kubo-Toyabe relaxation function $G_{\text{KT}} = [\frac{1}{3} + \frac{2}{3}(1 - \sigma_{\text{ZF}}^2 t^2) e^{-\frac{\sigma_{\text{ZF}}^2 t^2}{2}}]$ ^{42,43}. The solid lines in Fig 13 represent fits to the data by considering an additional zero-field Lorentzian relaxation Λ , i.e., $A_{\text{ZF}} = A_s G_{\text{KT}} e^{-\Lambda t} + A_{\text{bg}}$. Here A_s and A_{bg} are the same as in the TF- μSR case [see Eq. (3)]. The strong Gaussian relaxation rates reflect the large nuclear moments in $\text{Nb}_5\text{Ir}_{3-x}\text{Pt}_x\text{O}$, mostly determined by the Nb nuclear moments. In both the normal- and the superconducting states, the relaxations are almost identical, as demonstrated by the practically overlapping ZF- μSR

spectra above and below T_c . This lack of evidence for an ad-

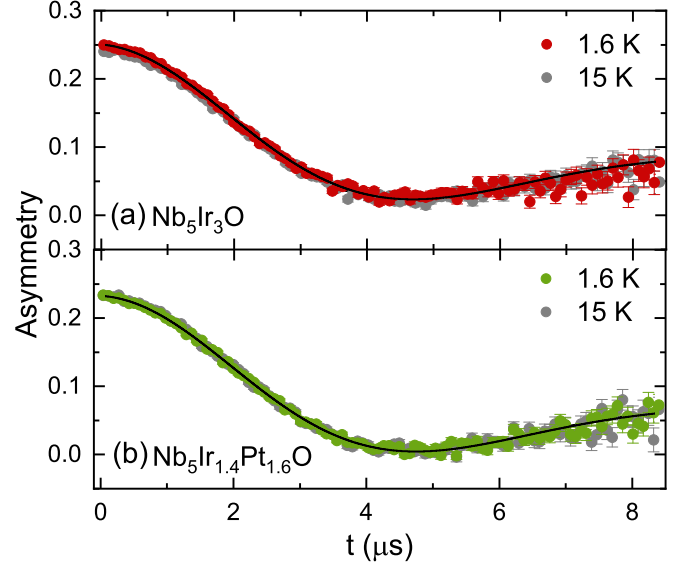


FIG. 13. ZF- μSR spectra for $\text{Nb}_5\text{Ir}_3\text{O}$ (a) and $\text{Nb}_5\text{Ir}_{1.4}\text{Pt}_{1.6}\text{O}$ (b) in the superconducting (1.6 K) and the normal state (15 K). Solid lines are fits to the equation described in the text. None of the datasets shows clear changes with temperature.

ditional μSR relaxation below T_c excludes a possible time-reversal symmetry breaking in the superconducting state of $\text{Nb}_5\text{Ir}_{3-x}\text{Pt}_x\text{O}$.

IV. CONCLUSION

To summarize, we investigated the superconducting properties of $\text{Nb}_5\text{Ir}_{3-x}\text{Pt}_x\text{O}$ (for $x = 0$ and 1.6) by means of electrical resistivity, magnetization, specific heat, and μSR measurements. $\text{Nb}_5\text{Ir}_3\text{O}$ and $\text{Nb}_5\text{Ir}_{1.4}\text{Pt}_{1.6}\text{O}$ exhibit bulk T_c at 10.5 and 9.1 K, respectively. The temperature dependence of the zero-field electronic specific heat and superfluid density reveal a nodeless SC in $\text{Nb}_5\text{Ir}_{3-x}\text{Pt}_x\text{O}$, well described by an isotropic s -wave model. $\text{Nb}_5\text{Ir}_3\text{O}$, instead, turns out to be a multigap superconductor, as demonstrated by the field dependence of the electronic specific heat coefficient, the superconducting Gaussian relaxation, and the temperature dependence of its upper critical field. Upon Pt substitution, the small superconducting gap is suppressed and $\text{Nb}_5\text{Ir}_{1.4}\text{Pt}_{1.6}\text{O}$ shows typical features of single gap SC, hence indicating a crossover from multiple- to single gap SC in the $\text{Nb}_5\text{Ir}_{3-x}\text{Pt}_x\text{O}$ family. Finally, the lack of spontaneous magnetic fields below T_c indicates that the time-reversal symmetry is preserved in $\text{Nb}_5\text{Ir}_{3-x}\text{Pt}_x\text{O}$ superconductors.

ACKNOWLEDGMENTS

The authors thank R. Khassanov for fruitful discussions and acknowledge the assistance from the $S\mu\text{S}$ beamline scientists. This work was supported by the Schweizerische Nationalfonds zur Förderung der Wissenschaftlichen Forschung, SNF (Grants No. 200021_169455 and 206021_139082).

- * Corresponding author: yangxu@physik.uzh.ch
† Corresponding author: tian.shang@psi.ch
- ¹ Y. Zhang, B. Wang, Z. Xiao, Y. Lu, T. Kamiya, Y. Uwatoko, H. Kageyama, and H. Hosono, Electride and superconductivity behaviors in Mn_5Si_3 -type intermetallics, *npj Quant. Mater.* **2**, 45 (2017).
 - ² B. Cort, A. L. Giorgi, and G. R. Stewart, Low temperature specific heats of $H(NbIrO)$ and $R(NbPtO)$, *J. Low Temp. Phys.* **47**, 179 (1982).
 - ³ S. Hamamoto and J. Kitagawa, Superconductivity in oxygen-added Zr_5Pt_3 , *Mater. Res. Express* **5**, 106001 (2018).
 - ⁴ A. D. Bortolozzo, C. A. M. dos Santos, R. F. Jardim, C. Ritter, A. Devishvili, M. Rotter, F. G. Gandra, and A. J. S. Machado, Interstitial doping induced superconductivity at 15.3 K in Nb_5Ge_3 compound, *J. Appl. Phys.* **111**, 123912 (2012).
 - ⁵ S. T. Renosto, R. Lang, A. L. R. Manesco, D. Rodrigues Jr., F. B. Santos, A. J. S. Machado, M. R. Baldan, and E. Diez, Strong Electronic Interaction and Signatures of Nodal Superconductivity in $Zr_5Pt_3C_x$, *arXiv preprint arXiv:1809.05008* (2018).
 - ⁶ B. Wang, Y. Zhang, S. Xu, K. Ishigaki, K. Matsubayashi, J.-G. Cheng, H. Hosono, and Y. Uwatoko, Robust two-gap strong coupling superconductivity associated with low-lying phonon modes in pressurized Nb_5Ir_3O superconductors, *Chinese Phys. B* **28**, 107401 (2019).
 - ⁷ B. Lv, X. Y. Zhu, B. Lorenz, F. Y. Wei, Y. Y. Xue, Z. P. Yin, G. Kotliar, and C. W. Chu, Superconductivity in the Mn_5Si_3 -type Zr_5Sb_3 system, *Phys. Rev. B* **88**, 134520 (2013).
 - ⁸ J. Kitagawa and S. Hamamoto, Superconductivity in $Nb_5Ir_{3-x}Pt_xO$, *arXiv preprint arXiv:1910.00686* (2019).
 - ⁹ A. Amato, H. Luetkens, K. Sedlak, A. Stoykov, R. Scheuermann, M. Elender, A. Raselli, and D. Graf, The new versatile general purpose surface-muon instrument (GPS) based on silicon photomultipliers for μ SR measurements on a continuous-wave beam, *Rev. Sci. Instrum.* **88**, 093301 (2017).
 - ¹⁰ A. Suter and B. M. Wojek, Musrfit: A free platform-independent framework for μ SR data analysis, *Phys. Procedia* **30**, 69 (2012).
 - ¹¹ X. Zhu, H. Yang, L. Fang, G. Mu, and H.-H. Wen, Upper critical field, Hall effect and magnetoresistance in the iron-based layered superconductor $LaFeAsO_{0.9}F_{0.1-\delta}$, *Supercond. Sci. Technol.* **21**, 105001 (2008).
 - ¹² N. R. Werthamer, E. Helfand, and P. C. Hohenberg, Temperature and purity dependence of the superconducting critical field, H_{c2} . III. Electron spin and spin-orbit effects, *Phys. Rev.* **147**, 295 (1966).
 - ¹³ E. H. Brandt, Properties of the ideal Ginzburg-Landau vortex lattice, *Phys. Rev. B* **68**, 054506 (2003).
 - ¹⁴ C. Kittel, *Introduction to Solid State Physics*, 8th ed. (John Wiley & Sons, Hoboken, NJ, 2005).
 - ¹⁵ W. L. McMillan, Transition temperature of strong-coupled superconductors, *Phys. Rev.* **167**, 331 (1968).
 - ¹⁶ C. H. P. Wen, H. C. Xu, Q. Yao, R. Peng, X. H. Niu, Q. Y. Chen, Z. T. Liu, D. W. Shen, Q. Song, X. Lou, Y. F. Fang, X. S. Liu, Y. H. Song, Y. J. Jiao, T. F. Duan, H. H. Wen, P. Dudin, G. Kotliar, Z. P. Yin, and D. L. Feng, Unveiling the superconducting mechanism of $Ba_{0.51}K_{0.49}BiO_3$, *Phys. Rev. Lett.* **121**, 117002 (2018).
 - ¹⁷ T. Shang, D. J. Gawryluk, M. Naamneh, Z. Salman, Z. Guguchia, M. Medarde, M. Shi, N. C. Plumb, and T. Shiroka, Strong- to weak-coupling superconductivity in high- T_c bismuthates: Revisiting the phase diagram via μ SR, *Phys. Rev. B* **101**, 014508 (2020).
 - ¹⁸ T. P. Ying, Y. P. Qi, and H. Hosono, Superconductivity with strong electron-phonon coupling in noncentrosymmetric W_3Al_2C , *Phys. Rev. B* **100**, 094522 (2019).
 - ¹⁹ M. Tinkham, *Introduction to Superconductivity*, 2nd ed. (Dover Publications, Mineola, NY, 1996).
 - ²⁰ H. Padamsee, J. E. Neighbor, and C. A. Shiffman, Quasiparticle phenomenology for thermodynamics of strong-coupling superconductor, *J. Low Temp. Phys.* **12**, 387 (1973).
 - ²¹ A. Carrington and F. Manzano, Magnetic penetration depth of MgB_2 , *Physica C* **385**, 205 (2003).
 - ²² A. Maisuradze, R. Khasanov, A. Shengelaya, and H. Keller, Comparison of different methods for analyzing μ SR line shapes in the vortex state of type-II superconductors, *J. Phys.: Condens. Matter* **21**, 075701 (2009), and references therein.
 - ²³ W. Barford and J. M. F. Gunn, The theory of the measurement of the London penetration depth in uniaxial type II superconductors by muon spin rotation, *Physica C* **156**, 515 (1988).
 - ²⁴ C. Niedermayer, C. Bernhard, T. Holden, R. K. Kremer, and K. Ahn, Muon spin relaxation study of the magnetic penetration depth in MgB_2 , *Phys. Rev. B* **65**, 094512 (2002).
 - ²⁵ T. Shang, A. Amon, D. Kasinathan, W. Xie, M. Bobnar, Y. Chen, A. Wang, M. Shi, M. Medarde, H. Q. Yuan, and T. Shiroka, Enhanced t_c and multiband superconductivity in the fully-gapped $ReBe_{22}$ superconductor, *New J. Phys.* **21**, 073034 (2019).
 - ²⁶ J. Chen, L. Jiao, J. L. Zhang, Y. Chen, L. Yang, M. Nicklas, F. Steglich, and H. Q. Yuan, Evidence for two-gap superconductivity in the non-centrosymmetric compound $LaNiC_2$, *New J. Phys.* **15**, 053005 (2013).
 - ²⁷ J. T. Chen, Y. Sun, T. Yamada, S. Pyon, and T. Tamegai, Two-gap features revealed by specific heat measurements in $FeSe$, *J. Phys. Conf. Ser.* **871**, 012016 (2017).
 - ²⁸ F. Bouquet, R. A. Fisher, N. E. Phillips, D. G. Hinks, and J. D. Jorgensen, Specific heat of $Mg^{11}B_2$: Evidence for a second energy gap, *Phys. Rev. Lett.* **87**, 047001 (2001).
 - ²⁹ T. Shang, M. Smidman, S. K. Ghosh, C. Baines, L. J. Chang, D. J. Gawryluk, J. A. T. Barker, R. P. Singh, D. M. Paul, G. Balakrishnan, E. Pomjakushina, M. Shi, M. Medarde, A. D. Hillier, H. Q. Yuan, J. Quintanilla, J. Mesot, and T. Shiroka, Time-Reversal Symmetry Breaking in Re-Based Superconductors, *Phys. Rev. Lett.* **121**, 257002 (2018).
 - ³⁰ C. Caroli, P. G. De Gennes, and J. Matricon, Bound Fermion states on a vortex line in a type II superconductor, *Phys. Lett.* **9**, 307 (1964).
 - ³¹ G. E. Volovik, Superconductivity with lines of gap nodes: density of states in the vortex, *JETP Lett.* **58**, 469 (1993).
 - ³² H.-H. Wen, Z.-Y. Liu, F. Zhou, J. Xiong, W. Ti, T. Xiang, S. Komiya, X. Sun, and Y. Ando, Electronic specific heat and low-energy quasiparticle excitations in the superconducting state of $La_{2-x}Sr_xCuO_4$ single crystals, *Phys. Rev. B* **70**, 214505 (2004).
 - ³³ S. Serventi, G. Allodi, R. De Renzi, G. Guidi, L. Romanò, P. Manfrinetti, A. Palenzona, C. Niedermayer, A. Amato, and C. Baines, Effect of Two Gaps on the Flux-lattice Internal Field Distribution: Evidence of Two Length Scales in $Mg_{1-x}Al_xB_2$ from μ SR, *Phys. Rev. Lett.* **93**, 217003 (2004).
 - ³⁴ R. Khasanov, A. Amato, P. K. Biswas, H. Luetkens, N. D. Zhigadlo, and B. Batlogg, $SrPt_3P$: A two-band single-gap superconductor, *Phys. Rev. B* **90**, 140507(R) (2014).
 - ³⁵ K.-H. Müller, G. Fuchs, A. Handstein, K. Nenkov, V. N. Narozhnyi, and D. Eckert, The upper critical field in superconducting MgB_2 , *J. Alloys Compd.* **322**, L10 (2001).
 - ³⁶ A. Gurevich, S. Patnaik, V. Braccini, K. H. Kim, C. Mielke, X. Song, L. D. Cooley, S. D. Bu, D. M. Kim, J. H. Choi, L. J. Belenky, J. Giencke, M. K. Lee, W. Tian, X. Q. Pan, A. Siri, E. E. Hellstrom, C. B. Eom, and D. C. Larbalestier, Very high upper critical fields in MgB_2 produced by selective tuning of impurity scattering, *Supercond. Sci. Technol.* **17**, 278 (2004).
 - ³⁷ A. Gurevich, Iron-based superconductors at high magnetic fields, *Rep. Prog. Phys.* **74**, 124501 (2011), and references therein.
 - ³⁸ T. Shiroka, T. Shang, C. Wang, G.-H. Cao, I. Eremin, H.-R. Ott, and J. Mesot, High- T_c superconductivity in undoped $ThFeAsN$,

- [Nat. Commun. 8, 156 \(2017\)](#).
- ³⁹ Y. J. Uemura, L. P. Le, G. M. Luke, B. J. Sternlieb, W. D. Wu, J. H. Brewer, T. M. Riseman, C. L. Seaman, M. B. Maple, M. Ishikawa, D. G. Hinks, J. D. Jorgensen, G. Saito, and H. Yamochi, Basic similarities among cuprate, bismuthate, organic, Chevrel-phase, and heavy-fermion superconductors shown by penetration-depth measurements, [Phys. Rev. Lett. 66, 2665 \(1991\)](#).
- ⁴⁰ Y. J. Uemura, Twin spin/charge roton mode and superfluid density: Primary determining factors of T_c in high- T_c superconductors observed by neutron, ARPES, and μ SR, [Physica B 374, 1 \(2006\)](#).
- ⁴¹ J. A. T. Barker, B. D. Breen, R. Hanson, A. D. Hillier, M. R. Lees, G. Balakrishnan, D. M. Paul, and R. P. Singh, Superconducting and normal-state properties of the noncentrosymmetric superconductor Re_3Ta , [Phys. Rev. B 98, 104506 \(2018\)](#), and references therein.
- ⁴² R. Kubo and T. Toyabe, A stochastic model for low field resonance and relaxation, in *Magnetic Resonance and Relaxation*, edited by R. Blinc (North-Holland, Amsterdam, 1967) p. 810.
- ⁴³ A. Yaouanc and P. D. de Réotier, *Muon Spin Rotation, Relaxation, and Resonance: Applications to Condensed Matter* (Oxford University Press, Oxford, 2011).